

AD-A279 238



12

AD

TECHNICAL REPORT ARCCB-TR-94007

A STRESS FACTOR METHOD FOR PERFORATED MUZZLE BRAKE DESIGN

GARRY C. CAROFANO
MARTIN R. LEACH

DTIC
SELECTED
MAY 17, 1994
S B D

FEBRUARY 1994



US ARMY ARMAMENT RESEARCH,
DEVELOPMENT AND ENGINEERING CENTER
CLOSE COMBAT ARMAMENTS CENTER
BENÉT LABORATORIES
WATERVLIET, N.Y. 12189-4050



THIS COPY IS UNCLASSIFIED

APPROVED FOR PUBLIC RELEASE; DISTRIBUTION UNLIMITED

94-14658



94 5 16 114

DISCLAIMER

The findings in this report are not to be construed as an official Department of the Army position unless so designated by other authorized documents.

The use of trade name(s) and/or manufacturer(s) does not constitute an official indorsement or approval.

DESTRUCTION NOTICE

For classified documents, follow the procedures in DoD 5200.22-M, Industrial Security Manual, Section II-19 or DoD 5200.1-R, Information Security Program Regulation, Chapter IX.

For unclassified, limited documents, destroy by any method that will prevent disclosure of contents or reconstruction of the document.

For unclassified, unlimited documents, destroy when the report is no longer needed. Do not return it to the originator.

Accession For	
NTIS GRAAI <input checked="" type="checkbox"/>	
DTIG TAB <input type="checkbox"/>	
Unannounced <input type="checkbox"/>	
Justification	
By _____	
Distribution _____	
Availability Dates	
Date	Serial and/or
	Special

REPORT DOCUMENTATION PAGE

Form Approved
OMB No. 0704-0188

Public reporting burden for this collection of information is estimated to average 1 hour per response, including the time for reviewing instructions, searching existing data sources, gathering and maintaining the data needed, and completing and reviewing the collection of information. Send comments regarding this burden estimate or any other aspect of this collection of information, including suggestions for reducing this burden, to Washington Headquarters Services, Directorate for Information Operations and Reports, 1215 Jefferson Davis Highway, Suite 1204, Arlington, VA 22202-4302, and to the Office of Management and Budget, Paperwork Reduction Project (0704-0188), Washington, DC 20503.

1. AGENCY USE ONLY (Leave blank)			2. REPORT DATE	3. REPORT TYPE AND DATES COVERED
			February 1994	Final
4. TITLE AND SUBTITLE A STRESS FACTOR METHOD FOR PERFORATED MUZZLE BRAKE DESIGN			5. FUNDING NUMBERS AMCMS: 611.02.H611.100	
6. AUTHOR(S) Garry C. Carofano and Martin R. Leach				
7. PERFORMING ORGANIZATION NAME(S) AND ADDRESS(ES) U.S. Army ARDEC Benét Laboratories Watervliet, NY 12189-4050			8. PERFORMING ORGANIZATION REPORT NUMBER ARCCB-TR-94007	
9. SPONSORING/MONITORING AGENCY NAME(S) AND ADDRESS(ES) U.S. Army ARDEC Close Combat Armaments Center Picatinny Arsenal, NJ 07806-5000			10. SPONSORING/MONITORING AGENCY REPORT NUMBER	
11. SUPPLEMENTARY NOTES Accepted for presentation at the 1994 ASME Pressure Vessel and Piping Conference, 19-23 June 1994, Minneapolis, MN. Accepted for publication in the Conference Proceedings.				
12a. DISTRIBUTION / AVAILABILITY STATEMENT Approved for public release; distribution unlimited			12b. DISTRIBUTION CODE	
13. ABSTRACT (Maximum 200 words) A perforated muzzle brake consists of a set of vents drilled through the wall of a cannon near the muzzle to reduce the impulse transmitted to the mount. The vented structure must support both the tube pressure and the pressure acting on the vent surfaces that produces the braking force. This report presents a method for estimating the maximum Von Mises stress within the structure. The results agree to within 10 percent of those from a more detailed finite element calculation.				
14. SUBJECT TERMS Gun, Muzzle Brake, Cylinder With Multiple Holes, Stress Factors			15. NUMBER OF PAGES 15	16. PRICE CODE
17. SECURITY CLASSIFICATION OF REPORT UNCLASSIFIED		18. SECURITY CLASSIFICATION OF THIS PAGE UNCLASSIFIED	19. SECURITY CLASSIFICATION OF ABSTRACT UNCLASSIFIED	20. LIMITATION OF ABSTRACT U

TABLE OF CONTENTS

INTRODUCTION	1
GASDYNAMICS ANALYSIS	1
STRESS ANALYSIS	2
RESULTS AND DISCUSSION	3
COMPARISON OF THE TWO MODELS	4
SUMMARY AND CONCLUSIONS	5
REFERENCES	5
APPENDIX A	6
APPENDIX B	6

Tables

1. Dimensionless Parameters Describing Vent Geometry	3
2. Stress Factors	3
A1. Vent Pressure Distribution, $p(\theta, Z)/p_e$	6
B1. Coefficients, k_m , in Eq. (B1) for $n_c = 10$	7
B2. Coefficients, k_m , in Eq. (B1) for $n_c = 12$	7

List of Illustrations

1. A PERFORATED MUZZLE BRAKE	8
2. PRESSURE CONTOUR AND VELOCITY VECTOR PLOTS FOR A SINGLE VENT AT THE BRAKE ENTRANCE	8
3. VENT PRESSURE DISTRIBUTIONS	9
4. THE COLUMN MODEL (a) AND THE SINGLE VENT MODEL (b)	10
5. VENT NOMENCLATURE	10
6. STRESS FACTORS FOR $r_o/r_b = 1.35$ and $n_c = 12$	11
7. SINGLE VENT MODEL SHOWING CIRCUMFERENTIAL WEB DISTORTION	12
8. COMPARISON OF THE VON MISES STRESS FOR BOTH MODELS	12

9. COMPARISON OF THE VON MISES STRESS FOR BOTH MODELS	13
10. COMPARISON OF THE VON MISES STRESS FOR BOTH MODELS	13

A STRESS FACTOR METHOD FOR PERFORATED MUZZLE BRAKE DESIGN

Garry C. Carofano and Martin R. Leach
U.S. Army Armament Research, Development, and Engineering Center
Close Combat Armaments Center
Benét Laboratories
Watervliet, NY

ABSTRACT

A perforated muzzle brake consists of a set of vents drilled through the wall of a cannon near the muzzle to reduce the impulse transmitted to the mount. The vented structure must support both the tube pressure and the pressure acting on the vent surfaces that produces the braking force. This report presents a method for estimating the maximum Von Mises stress within the structure. The results agree to within 10 percent of those from a more detailed finite element calculation.

INTRODUCTION

Perforated muzzle brakes reduce the axial thrust of the propellant gas flowing from the muzzle by venting some of the gas through the cannon wall (see Figure 1). The pressure distribution in each vent is asymmetric with the highest pressure acting on the downstream surface, hence, a net axial force is developed. The left end of the vented region, called the brake entrance, must support the total brake load and the maximum internal pressure. In practice, an iterative process is used to find a vent pattern which will produce sufficient braking without exceeding a specified stress level. Since the flow and stress fields are three-dimensional, some simplification is needed to make the process practical. An approximate method for solving the stress problem is presented here that parallels the approach used in a previous analysis of the flow problem.

GASDYNAMICS ANALYSIS

Earlier work (Nagamatsu et al. 1987; Carofano 1988) considered the three-dimensional flow at the brake entrance. Because the vents are placed symmetrically

around the tube, the analysis was restricted to a single vent and the portion of the tube volume associated with it. The characteristic time for tube blowdown is determined by the cannon length, while the time to establish the vent flow is proportional to the tube wall thickness, a much smaller value. Therefore, the vent flow was treated as quasi-steady. The flowfield and pressure distribution presented in this section were obtained using the computer model described by Nagamatsu et al. (1987) and Carofano (1988).

The velocity vector and pressure contour plots in Figure 2 show a typical flow pattern in the symmetry plane of the vent. A uniform flow enters the brake at Mach number, $M=1.5$, and accelerates as a portion of the gas expands and turns into the vent. The shock at the downstream lip of the vent turns the expanded flow parallel to the solid surfaces and reduces the velocities to subsonic levels. The solid lines in the vector plot indicate where the local Mach number is unity. The flow in the tube accelerates away from this region and leaves the grid at supersonic velocities. Because the tube pressure is well above ambient, the flow is also supersonic over most of the vent exit area and was found to be insensitive to the extrapolated boundary condition used over the subsonic portion. For the Euler equations, then, the flow is independent of events occurring farther downstream or in the surroundings and is completely described by the vent geometry and the Mach number and thermodynamic properties of the gas upstream of it. One solution with these parameters specified is valid for all pressures and densities. Average values of the mass flux at the vent exit were obtained as functions of the parameters. This information was used to construct a source term in the one-dimensional time-dependent Euler equations which relates the local vent flow rate at a specific axial location to the local vent area and the pressure and density. The equations were numerically integrated over the length of the cannon, starting from a time

when the projectile base is just upstream of the brake entrance and ending with the completion of the blowdown process.

The vent pressure distribution is needed for the stress analysis. It is a function of the vent geometry and the local pressure and Mach number in the tube. The dependence on Mach number is shown in Figure 3a for a geometry having a height-to-diameter ratio, h/d , of unity. The abscissa, z/d , is the dimensionless distance through the tube wall measured from the bore surface. The ordinate, p/p_{∞} , is the local pressure divided by the uniform pressure at the brake entrance. The two curves in each plot correspond to brake entrance Mach numbers of 1.0 and 1.5. The higher Mach number produces a greater pressure on the downstream surface behind the shock but is of little significance elsewhere.

The effect of vent geometry, h/d , is confined to the upstream wall, as shown in Figure 3b. The pressure level is higher for the taller vent ($h/d=1.25$) because the gas actually swirls around the vent surface as it flows radially outward and is compressed at the upstream wall (ref 1). Note the stagnation point in Figure 2 and the recirculation zone below it. A vent with $h/d=1$ represents the crossover point where the net axial load on the vent surface starts to decrease with increasing height.

There are a number of other parameters that affect the stress field and, in view of the previous discussion, adding the Mach number and vent geometry to the list seems unnecessary. Instead, the pressure distribution corresponding to $M=1.5$ and $h/d=1$ was chosen. Based on internal ballistics solutions, this Mach number represents an upper limit at the brake entrance and will provide a conservative estimate of the maximum stress. Furthermore, since $h/d=1$ represents the optimum flow geometry, it will appear most often in design. The complete vent pressure distribution is tabulated in Appendix A.

The tube surface pressure distribution near the vent is also needed. It is uniform upstream because the brake entrance Mach number is supersonic. Downstream of the vent, it is nearly uniform (see Figure 2) and approximately equal to the entrance value. To simplify the analysis, the pressure was taken to be uniform over the entire surface area associated with the vent. Together with the vent pressure distribution, this completely defines the instantaneous loads on the brake for the stress field calculation.

STRESS ANALYSIS

Unlike the flow problem, the stress field near the brake entrance depends on conditions downstream because the total axial load is transmitted through this region. Also, the abrupt transition to a perforated structure dictates that a portion of the tube upstream of the entrance must be included in the analysis. While the symmetrical placement of the vents around the tube circumference means that

only one-half of one column has to be modeled (columns run axially), the computer memory for a practical brake is too large. As a compromise, two configurations were studied. The first is a column model that uses only a few vent rows at the brake entrance (rows run circumferentially) and an approximate boundary condition at the downstream end. This allows the transition effect to be modeled. The second considers a single vent in a pattern of geometrically similar vents in an infinite tube. This allows the effect of vent diameter and spacing to be calculated economically. The results are compared to column model predictions to determine if conservative estimates were obtained. The finite element structural analysis code ABAQUS was used for both models with a modulus of elasticity of 206.8 Gpa and Poisson's ratio equal to 0.29.

The column model is shown in Figure 4a. Approximately 14,000 second-order tetrahedron elements (ABAQUS C3D10) were used, each having 10 nodes. The left boundary was located one outside tube radius upstream of the brake entrance and was constrained to move in a fixed plane perpendicular to the tube axis. The right end was constrained to remain parallel to the left but free to move axially. Six vent rows were found to be sufficient to limit the influence of this artificial restraint on the results near the brake entrance. The surface pressure distributions used in the calculations are specified later.

The single vent model is shown in Figure 4b. Approximately 3500 second-order triangular prism elements (ABAQUS C3D15V) were used, each having 18 nodes. The vent was treated as one of an infinite set equally spaced on a tube. The left and right boundaries were constrained to remain geometrically similar under load. Solutions for the bore surface pressure, the axial load, and the vent pressure were obtained in separate steps. The results are then superimposed to obtain any desired loading.

A uniform bore surface pressure was applied in step I. The boundaries were constrained to be planar and normal to the tube axis. Equilibrium was maintained by restricting the left boundary to remain fixed. The right boundary was free to move axially.

In step II, the boundaries were treated as above except that the axial displacement of the right boundary was determined by setting the integrated axial load on this plane to a specified value. In a design problem, this is the total load generated by the vents farther downstream. The instantaneous load generated by each vent is given by the one-dimensional gasdynamics calculation of the blowdown process (Nagamatsu et al. 1987; Carofano 1988). This is demonstrated later with an example.

The vent pressure was applied in step III. Both boundaries were allowed to distort but in such a manner that they remained geometrically similar, consistent with the infinite geometry. To obtain a unique solution, additional information was required at the boundaries. It was desired to have the structure distort in response to the vent pressure distribution alone. The loads and displacements at the boundaries were to be part of the solution, not part of the

boundary conditions. This was achieved setting the sum of the axial displacements of the nodes on the left boundary equal to zero. Translatory rigid body motion was also avoided with this condition.

Solutions were obtained for sets of the parameters listed in Table 1. With reference to Figure 5, r_i and r_o are the inner and outer tube radii, respectively, d is the vent diameter, and x_c and s_c are the axial and circumferential vent spacings, respectively. s_c is defined as the arc length at the mid-wall radius $(r_o+r_b)/2$ that subtends the angle $\theta = 2\pi/n_c$ associated with each vent, or

$$s_c = \left(\frac{2\pi}{n_c} \right) \left(\frac{r_o+r_b}{2} \right) = \left(\frac{\pi r_b}{n_c} \right) (r_o/r_b + 1) \quad (1)$$

Current design practice led to the choices for the number of vent columns and the wall ratio. The vent spacings were chosen because they result in height-to-diameter ratios that span the optimum gasdynamic value of unity.

RESULTS AND DISCUSSION

The radial, tangential, and axial stress components are given at the three points on the edge where the bore and vent surfaces intersect, designated A, B, and C in Figure 4a. The calculated shear stresses at these points were found to be negligible. The components are used to calculate the Von Mises stress for arbitrary values of gas

pressure and axial loading. Experience with the column model showed that the maximum Von Mises stress always coincided with one of these points. The results are presented in the form of stress factors in Table 2. The negative numerical values, when multiplied by the gas pressure, p_g , give the compressive stresses acting on the tube and vent surfaces. The radial component corresponds to the uniform pressure at the bore surface. The tangential and axial components are taken from the vent pressure distribution tabulated in Appendix A.

The factor K_p is defined as

$$K_p = \frac{\sigma}{p_g \left(\frac{(r_d/r_b)^2 + 1}{(r_d/r_b)^2 - 1} \right)} \quad (2)$$

The stress, σ , is the sum of the contributions from steps I and III that result from the gas pressure loading. The denominator is the tangential stress at the bore surface of an unvented tube.

The factor K_t in Table 2 is associated with the axial loading in step II and is defined as

$$K_t = \frac{\sigma}{\left(\frac{L}{\pi r_b^2} \right) \left(\frac{1}{(r_d/r_b)^2 - 1} \right)} \quad (3)$$

The denominator is the axial stress in an unvented tube having the load, L , distributed uniformly at each end.

Table 1. Dimensionless Parameters Describing Vent Geometry

number of vent columns, n_c	10 and 12
wall ratio, r_i/r_o	1.35 and 1.45
axial spacing, d/x_c	0.50, 0.67 and 0.80
circumferential spacing, d/s_c	0.47, 0.55 and 0.66

Table 2. Stress Factors

Location	Gas Pressure Loading			Axial Loading		
	Radial	Tangential	Axial	Radial	Tangential	Axial
A	-1.0	K_{pA}	-2.208	0.0	K_{tA}	0.0
B	-1.0	-0.163	K_{pB}	0.0	0.0	K_{tB}
C	-1.0	K_{pC}	-0.081	0.0	K_{tC}	0.0

K_p and K_t are given in Figure 6 for a geometry having twelve vent columns and a wall ratio, $r_o/r_b = 1.35$. The abscissa in each plot is the circumferential spacing parameter, d/s_c . Each curve is for one value of the axial spacing parameter, d/x_c . The vent section in Figure 6c shows that stress factor K_{pA} applies at point A, which is located on the downstream lip of the vent on the bore surface, and similarly for the other factors. Because the loading is symmetrical in step II, K_{tC} is equal to K_{tA} and is not plotted.

The trend of the data is best understood by considering the load bearing area or web between vents relative to the unvented tube (see Figure 4a). For the circumferential direction, this is the ratio of the shaded area to total area in Figure 5, or

$$\frac{\text{circumferential web area}}{\text{total area}} = \frac{(s_c - d)(r_o - r_b)}{s_c(r_o - r_b)} = \left(1 - \frac{d}{s_c}\right) \quad (4)$$

As d/s_c increases, the web becomes thinner. Since the gas pressure and axial load were fixed in the analysis, the tangential stress factors K_{pA} , K_{pC} , and K_{tA} rise as d/s_c increases in magnitude from the lower to the upper curves in each plot. The area ratio is independent of d/s_c which explains the weak dependence on this parameter.

For the axial direction,

$$\frac{\text{axial web area}}{\text{total area}} = \frac{(s_c - d)(r_o - r_b)}{\pi(r_o^2 - r_b^2)/n_c} = \left(1 - \frac{d}{s_c}\right) \quad (5)$$

where Eq. (1) was used to simplify the expression. The web becomes thinner as d/s_c increases and the axial stress factors K_{pB} and K_{tB} increase accordingly. The area ratio is independent of d/s_c , so the weak dependence on this parameter is expected.

The results for the other combinations of the wall ratio, r_o/r_b , and the number of vent columns, n_c , do not differ appreciably from those in Figure 6 and are not plotted. Instead, they are given in polynomial form in Appendix B.

The finite element solution for step III is shown in Figure 7 for a geometry having a thin circumferential web. The view is from inside the tube looking at the bore surface. The vent surface is loaded asymmetrically by the gas pressure in this step and the thin web undergoes a large distortion near the bore surface. Interestingly, the tangential stress at point C exceeds that at point A, although the latter sees the high pressure behind the shock. This can be understood by recalling that the vent is one of an infinite set so that C also lies in the next vent downstream, on the same web with A. Both points are placed in tension, but the stress at C is higher. This is true for all of the thin web geometries, as shown by the upper curves in Figure 6a. The stress factors K_{pA} and K_{pC} include contributions from steps I and II, but these steps

produce symmetrical results. The difference between them is due to the asymmetrical loading in step III.

COMPARISON OF THE TWO MODELS

The gas pressure decreases with axial distance, x , through the brake due to venting. The comparison is made for a pressure of unity at the brake entrance and a pressure gradient equal to 5 percent per vent through the vented section. The column model has six rows of vents with uniform spacing, x_c , and an unvented section at the left of length, r_o , so the axial pressure distribution is

$$p_e = 1.0, \quad 0.0 \leq x \leq r_o, \quad (6)$$

$$p_e = 1.0 - 0.05(x - r_o)/x_c, \quad r_o < x \leq r_o + 6x_c$$

The vent pressure distribution in row number n is based on the average pressure, p_m , acting over the length x_c and is given by

$$p_m = 1.0 - 0.025(2n-1), \quad n = 1, 6 \quad (7)$$

To estimate the stresses using the single vent model, the axial load, L_n , applied to the downstream boundary of vent row number n is written as

$$L_n = (1/2) \sum_{m=n+1}^6 L_m, \quad n = 1, 5 \quad (8)$$

At the brake entrance, n is 1 and the five vents farther downstream each contribute an axial load L_m . At the sixth vent, L_6 is zero, since no load was applied at the right boundary in the column model. The factor 1/2 appears because the column model is made up of half-vents. L_m is the integral of the vent pressure distribution at vent number m and is shown in Appendix A to be

$$L_m = 0.9 (\pi d^2/4) p_m \quad (9)$$

p_m is the average pressure acting over the length x_c of vent m and is given by Eq. (7).

Since the shear stresses are negligible at the three points of interest, the Von Mises stress, σ_v , may be written as

$$\sigma_v = \sqrt{(\sigma_r - \sigma_o)^2 + (\sigma_t - \sigma_o)^2 + (\sigma_z - \sigma_o)^2} \quad (10)$$

where σ_r , σ_t , and σ_z are the radial, tangential, and axial stress components, respectively. These are given directly for the column model by the finite element solution. For the single vent model, they are computed using the stress factors in Table 2.

The following set of parameters was used:

$$\begin{aligned} r_d/r_b &= 1.35, \quad n_c = 12 \\ d/s_c &= 0.55, \quad d/x_c = 0.67 \end{aligned} \quad (11)$$

From Figure 6.

$$\begin{aligned} K_{PA} &= 2.76, \quad K_{LA} = -0.05 \\ K_{PB} &= 0.26, \quad K_{LB} = 3.03 \\ K_{PC} &= 2.75, \quad K_{LC} = -0.05 \end{aligned} \quad (12)$$

From Table 2, the stresses for points A, B, and C in vent number n are, respectively,

$$\sigma_r = -p_m \quad (13)$$

$$\sigma_t = K_{PA} \left(\frac{(r_d/r_b)^2 + 1}{(r_d/r_b)^2 - 1} \right) p_m + K_{LA} \left(\frac{1}{(r_d/r_b)^2 - 1} \right) \left(\frac{L_n}{\pi r_b^2} \right) p_m$$

$$\sigma_r = -p_m \quad (14)$$

$$\sigma_t = -2.208 p_m$$

$$\sigma_t = -0.163 p_m$$

$$\sigma_t = K_{PB} \left(\frac{(r_d/r_b)^2 + 1}{(r_d/r_b)^2 - 1} \right) p_m + K_{LB} \left(\frac{1}{(r_d/r_b)^2 - 1} \right) \left(\frac{L_n}{\pi r_b^2} \right) p_m$$

$$\sigma_r = -p_m \quad (15)$$

$$\sigma_t = K_{PC} \left(\frac{(r_d/r_b)^2 + 1}{(r_d/r_b)^2 - 1} \right) p_m + K_{LC} \left(\frac{1}{(r_d/r_b)^2 - 1} \right) \left(\frac{L_n}{\pi r_b^2} \right) p_m$$

$$\sigma_t = -0.081 p_m$$

Eqs. (1), (8), and (9) may be combined to give

$$\frac{L_n}{\pi r_b^2} = \left(\frac{0.9}{8} \right) \left(\frac{d}{s_c} \right) \left(\frac{\pi (r_d/r_b + 1)}{n_c} \right)^2 \sum_{m=n-1}^6 p_m \quad (16)$$

Eqs. (12) through (16) express the stress components in terms of the four dimensionless parameters and the local vent pressure.

The Von Mises stresses are plotted in Figure 8 for a geometry having comparable web thicknesses, as indicated by the vent figure in the upper right-hand corner. The solid and dashed lines represent the single vent and column models, respectively.

For the column model, the unvented section at the left provides support near the brake entrance that significantly reduces the stresses in the first vent at points A and C. At the right end, the results for vent 6 are obviously influenced by the boundary approximation and should be ignored.

The maximum stress in the column model occurs at point A in the second vent. Because of the nature of the single vent model, the maximum stress will always appear in the first vent. For this geometry and loading, the maximum is correctly predicted to lie at point A and is conservatively estimated with respect to the column model, exceeding the maximum in the latter by 10 percent. By "conservatively estimated," it is meant that the single vent prediction in the first vent exceeds the maximum stress occurring anywhere in the column model. This is the Von Mises stress that would be used in a failure criterion to check structural integrity.

For both models, the stress at point B is always highest at the brake entrance where the total axial load must be supported. The maximum stress in the column model exceeds the single vent estimate by 5 percent. If an axial load is imposed at the downstream end of either model, to simulate the addition of more vents, the stress at point B simply increases uniformly along the brake. The discrepancy at the brake entrance remains the same, although the stress at point B could become the maximum stress in the structure. For this geometry, the error is well within any reasonable choice for a safety factor.

To determine if the situation might worsen for one of the other geometries, two extremes were examined. The first considers the configuration having the thinnest axial web and the thickest circumferential web. As shown in Figure 9, the maximum stress occurs at point B and is conservatively estimated. At the opposite extreme, the thinnest circumferential web and the thickest axial web, the maximum stress occurs at point C, as shown in Figure 10, and is again conservatively estimated.

SUMMARY AND CONCLUSIONS

A stress factor method was presented for estimating the stress field in a perforated muzzle brake. The maximum Von Mises stress was found to occur at one of three critical locations depending upon the geometry and loading conditions. Compared with the results from a more detailed finite element calculation, the method predicts the location correctly and estimates the maximum stress to within 10 percent. The iteration time to find an acceptable design is significantly reduced. The final design can be checked using the more detailed model to assure structural integrity.

REFERENCES

Carofano, G.C. 1988. *The gasdynamics of perforated muzzle brakes*. ARCCB-TR-88006. Watervliet, NY: U.S. Army ARDEC, Benét Laboratories, February.

Nagamatsu, H.T., Choi, K.Y., Duffy, R.E., and Carofano, G.C. 1987. *An experimental and numerical study of the flow through a vent hole in a perforated muzzle brake.* ARCCB-TR-87016. Watervliet, NY: U.S. Army ARDEC, Benét Laboratories, June.

APPENDIX A

The vent pressure distribution, $p(\theta, Z)/p_\infty$, used in the analysis is given in Table A1. $p(\theta, Z)$ is the local wall pressure, p_∞ is the uniform pressure at the brake entrance, $Z = z/d$ is the dimensionless distance through the wall measured from the bore surface, and d is the vent diameter. θ is zero degrees on the downstream lip of the vent (point A in Figure 6c).

The integral of the vent pressure distribution, L_v , is

$$L_v = \left(\frac{\pi d^2}{4} \right) p_\infty \int_0^{\pi} \int_0^1 \frac{p(\theta, Z)}{p_\infty} \left(\frac{4}{\pi} \right) \cos(\theta) d\theta dZ = 0.9 \left(\frac{\pi d^2}{4} \right) \quad (A1)$$

APPENDIX B

The stress factors are given by the following polynomial:

$$K = 3.0 + C_1(d/x_c) + C_2(d/x_c)^2 + C_3(d/x_c)^3 \quad (B1)$$

where

$$C_1 = c_1 + c_2(d/s_c) + c_3(d/s_c)^2$$

$$C_2 = c_4 + c_5(d/s_c) + c_6(d/s_c)^2$$

$$C_3 = c_7 + c_8(d/s_c) + c_9(d/s_c)^2$$

and

$$c_n = k_{2n-1} + k_{2n}(r_s/r_c), n = 1, 9$$

The coefficients, k_m , $m=1, 18$, are given in Table B1 for $n_c=10$ and Table B2 for $n_c=12$. As an example, for a brake having ten columns of vents, the stress factor K_{PA} is computed from Eq. (B1) using the k 's in the second column of Table B1.

Table A1. Vent Pressure Distribution, $p(\theta, Z)/p_\infty$.

θ	Z									
	0.000	0.111	0.222	0.333	0.444	0.556	0.667	0.778	0.889	1.000
0	2.208	1.957	1.565	1.226	0.956	0.743	0.575	0.445	0.345	0.276
20	2.198	1.919	1.513	1.173	0.910	0.707	0.548	0.424	0.331	0.266
40	1.860	1.737	1.354	1.015	0.781	0.607	0.473	0.370	0.293	0.239
60	0.499	0.406	0.890	0.768	0.586	0.464	0.370	0.298	0.244	0.205
80	0.207	0.122	0.120	0.348	0.320	0.292	0.258	0.226	0.199	0.177
100	0.119	0.043	0.096	0.121	0.138	0.158	0.170	0.173	0.171	0.164
120	0.094	0.023	0.086	0.088	0.093	0.110	0.134	0.159	0.179	0.189
140	0.084	0.021	0.091	0.086	0.086	0.102	0.129	0.159	0.184	0.167
160	0.081	0.025	0.107	0.095	0.095	0.109	0.130	0.153	0.169	0.139
180	0.081	0.031	0.120	0.106	0.106	0.121	0.143	0.164	0.176	0.156

Table B1. Coefficients, k_m , in Eq. (B1) for $n_e=10$.

m	K_{PA}	K_{PB}	K_{PC}	K_{LA}	K_{LB}
1	9.752	32.208	20.249	-17.097	116.119
2	-5.042	-58.424	-22.639	0.900	-124.265
3	-59.674	-170.461	-49.987	-23.002	-535.074
4	67.375	204.136	75.967	13.057	571.614
5	24.631	204.160	11.010	43.786	588.101
6	-35.992	-239.545	-38.702	-47.052	-616.450
7	-33.002	-94.471	-88.450	44.462	-143.995
8	13.163	149.518	92.583	-19.943	134.020
9	206.175	415.876	178.664	28.687	744.062
10	-235.675	-516.342	-263.169	3.032	-735.554
11	-122.999	-459.704	-55.611	-106.586	-889.515
12	162.179	562.812	139.403	107.092	886.312
13	20.867	61.053	85.096	-36.848	42.308
14	1.151	-92.676	-84.260	27.252	-27.959
15	-167.704	-256.905	-161.741	19.808	-271.337
16	195.380	320.570	234.663	-50.472	235.248
17	117.576	275.544	57.362	42.909	367.002
18	-156.418	-340.425	-130.055	-33.577	-338.712

Table B2. Coefficients, k_m , in Eq. (B1) for $n_e=12$.

m	K_{PA}	K_{PB}	K_{PC}	K_{LA}	K_{LB}
1	6.663	19.853	20.415	-10.693	121.039
2	-0.819	-43.456	-20.862	-6.891	-131.410
3	-51.243	-120.767	-46.458	-46.448	-550.730
4	54.641	144.825	63.392	40.160	593.765
5	22.672	149.766	12.735	64.161	596.547
6	-33.743	-172.890	-34.682	-66.758	-631.213
7	-14.954	-74.147	-90.591	23.228	-162.969
8	-12.430	123.621	88.660	7.088	161.616
9	152.281	329.928	168.164	105.361	814.474
10	-155.102	-409.875	-224.793	-89.160	-834.153
11	-89.693	-362.327	-56.658	-172.140	-945.514
12	115.387	439.317	122.066	175.181	968.089
13	1.250	50.888	90.159	-20.796	57.827
14	28.758	-78.867	-85.660	6.212	-50.917
15	-107.376	-212.400	-161.200	-39.535	-332.212
16	104.768	262.499	213.466	23.474	322.146
17	73.775	223.902	61.571	95.141	420.618
18	-92.671	-272.306	-119.730	-91.351	-416.349

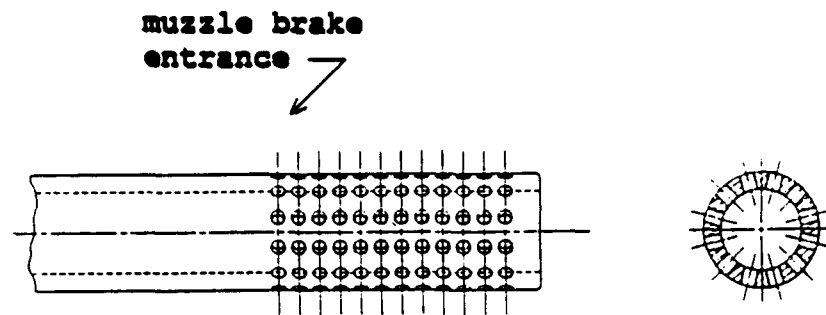


FIGURE 1. A PERFORATED MUZZLE BRAKE.

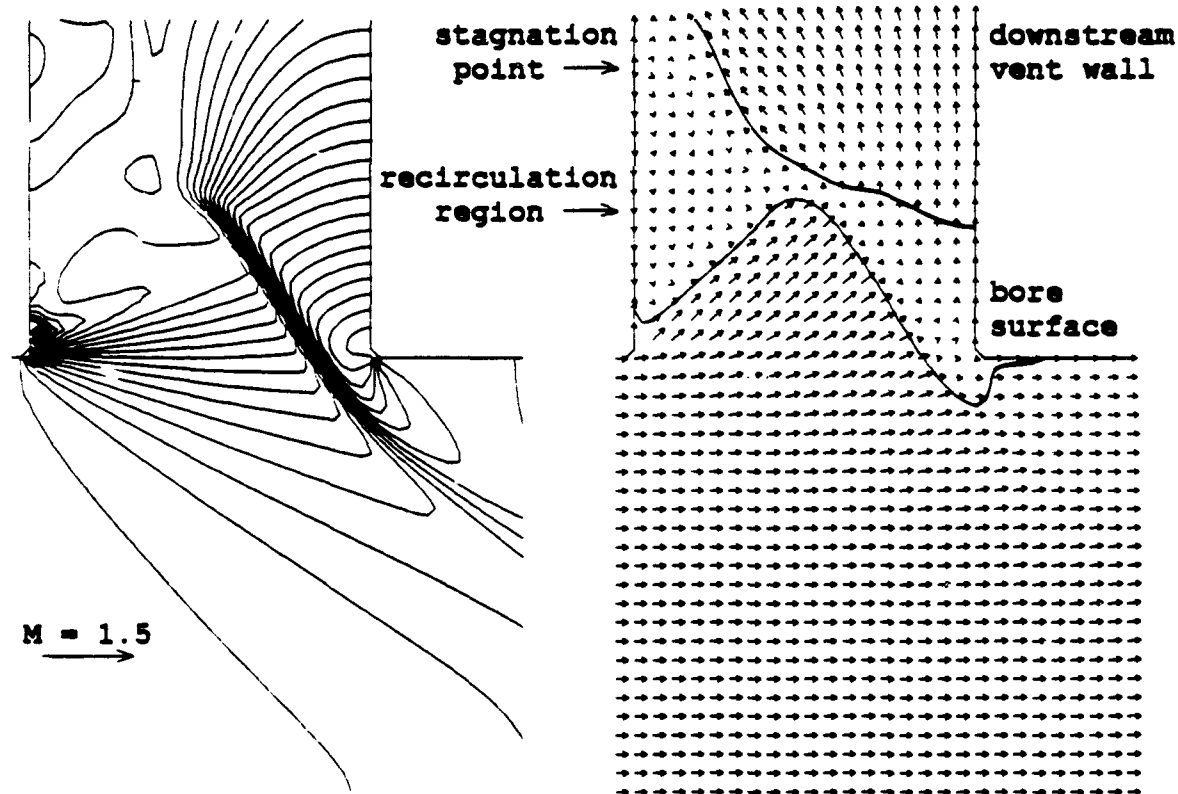
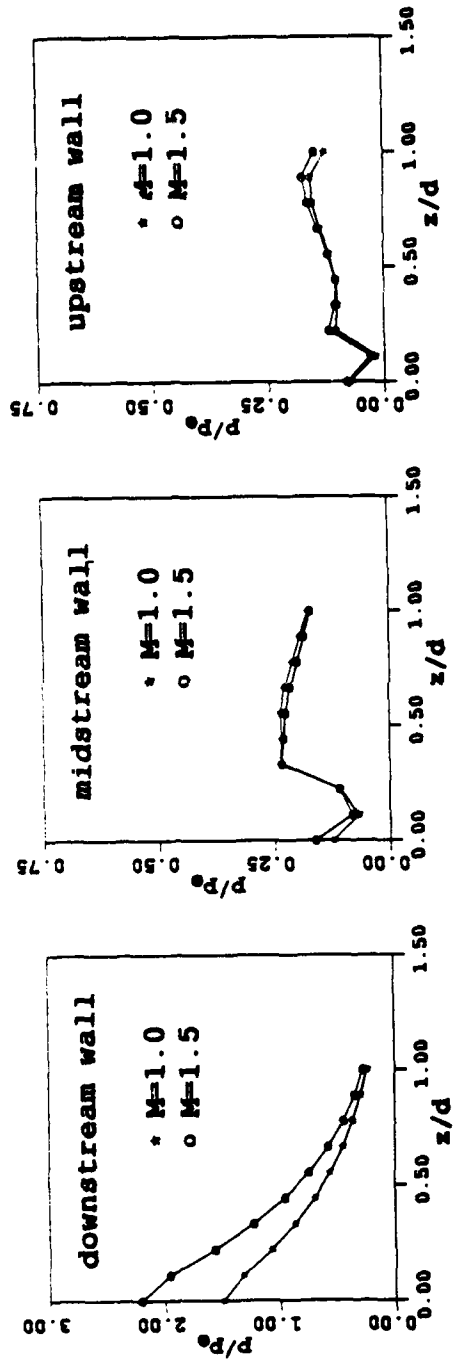


FIGURE 2. PRESSURE CONTOUR AND VELOCITY VECTOR PLOTS FOR A SINGLE VENT AT THE BRAKE ENTRANCE. THE SOLID LINES IN THE VECTOR PLOT INDICATE A MACH NUMBER OF UNITY.

(a) Effect of Mach number on vent pressure for $h/d=1$.



(b) Effect of h/d on vent pressure for $M=1.5$.

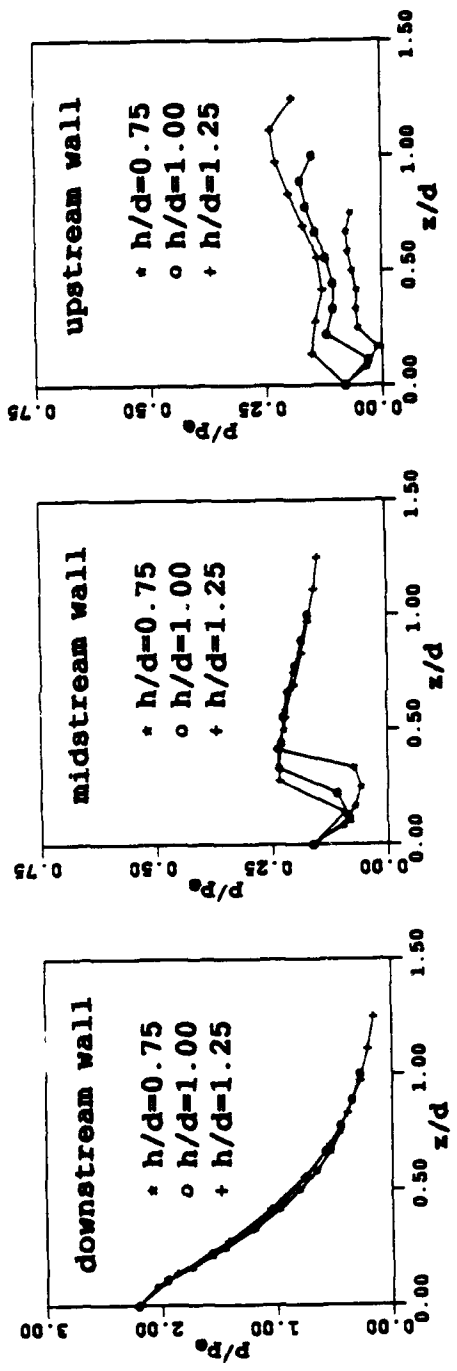


FIGURE 3. VENT PRESSURE DISTRIBUTIONS.

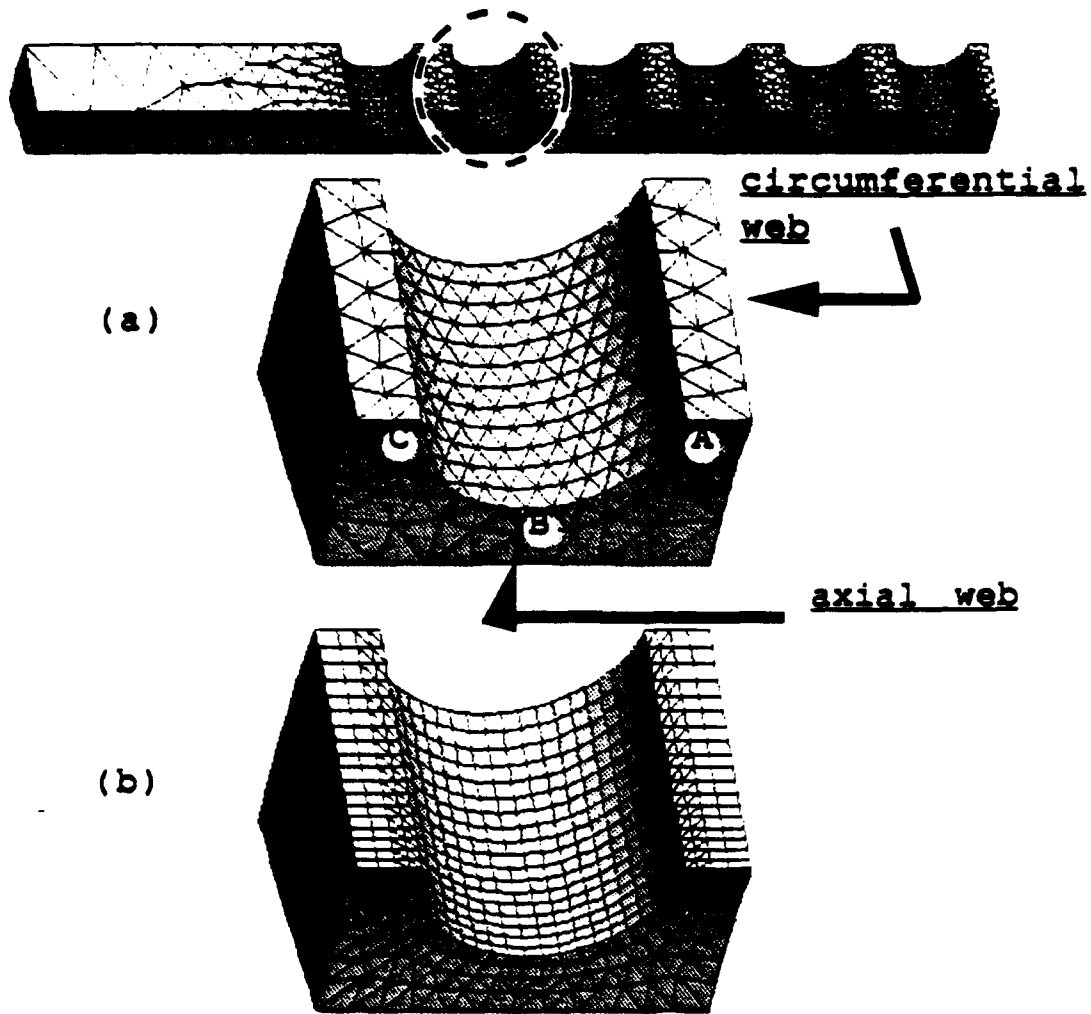


FIGURE 4. THE COLUMN MODEL (a) AND THE SINGLE VENT MODEL (b).
THE BORE SURFACE IS AT THE BOTTOM OF EACH MODEL.

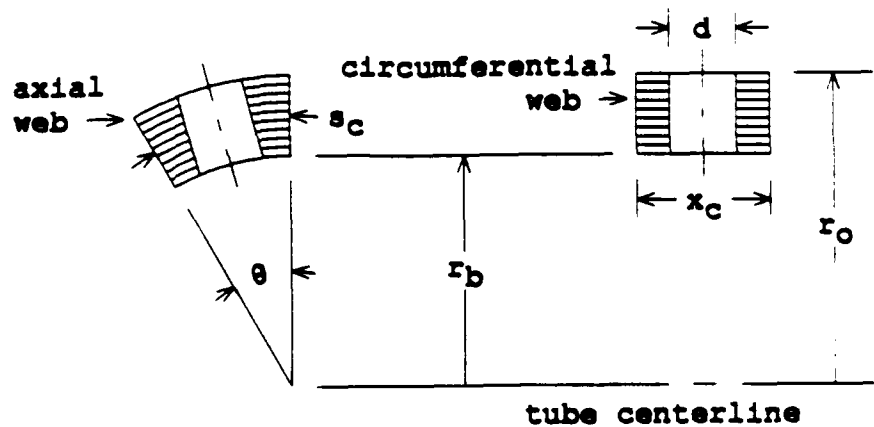
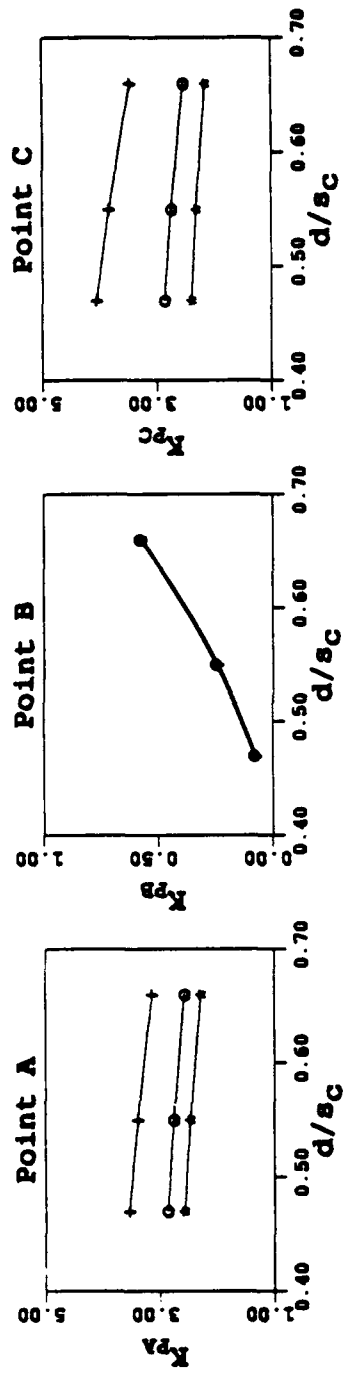


FIGURE 5. VENT NOMENCLATURE. THE WEB IS THE TOTAL SHADeD AREA IN EACH SECTION.

(a) Stress factors for gas pressure loading.



(b) Stress factors for axial loading.

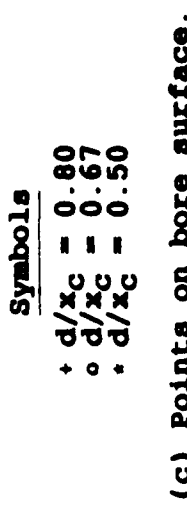
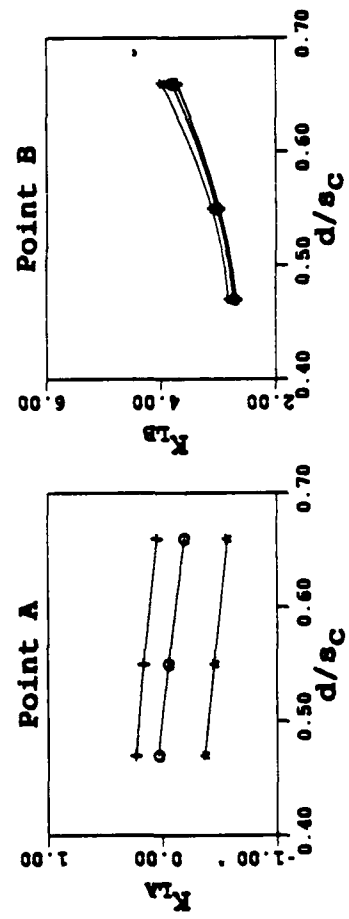


FIGURE 6. STRESS FACTORS FOR $r_d/r_b = 1.35$ and $n_c = 12$.

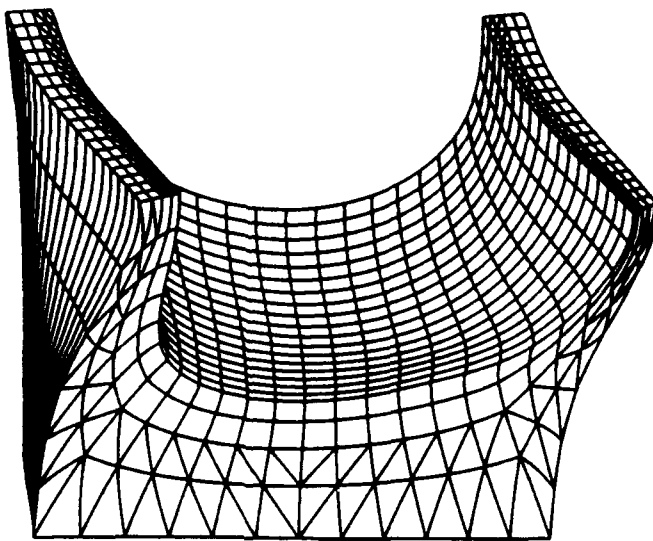


FIGURE 7. SINGLE VENT MODEL SHOWING CIRCUMFERENTIAL WEB DISTORTION. PARAMETERS ARE $r_o/r_b = 1.35$, $n_c = 12$, $d/s_c = 0.47$, AND $d/x_c = 0.80$.

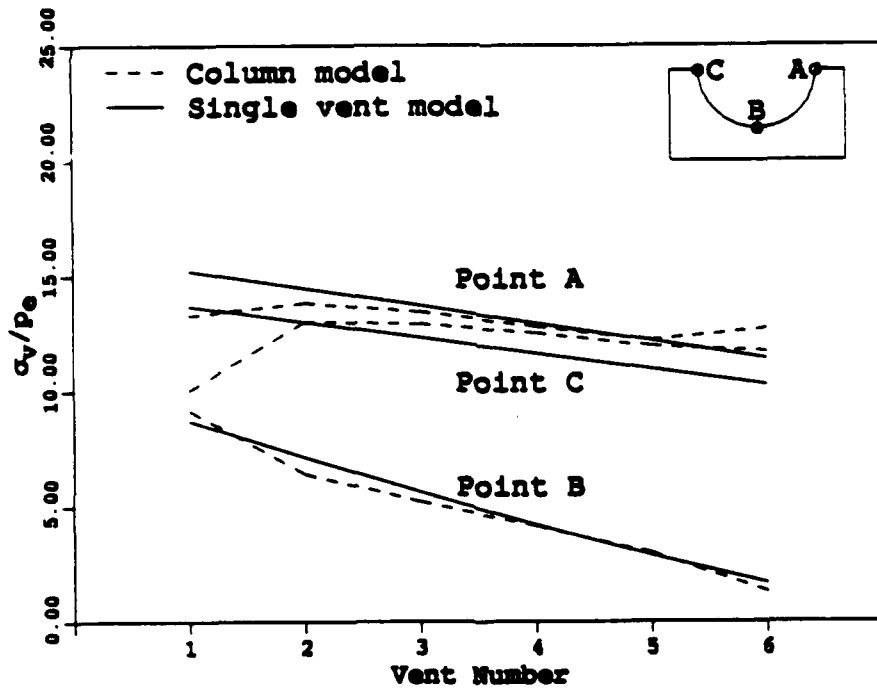


FIGURE 8. COMPARISON OF THE VON MISES STRESS FOR BOTH MODELS. VENT NUMBER 1 IS AT BRAKE ENTRANCE. $r_o/r_b = 1.35$, $n_c = 12$, $d/s_c = 0.55$, and $d/x_c = 0.67$.

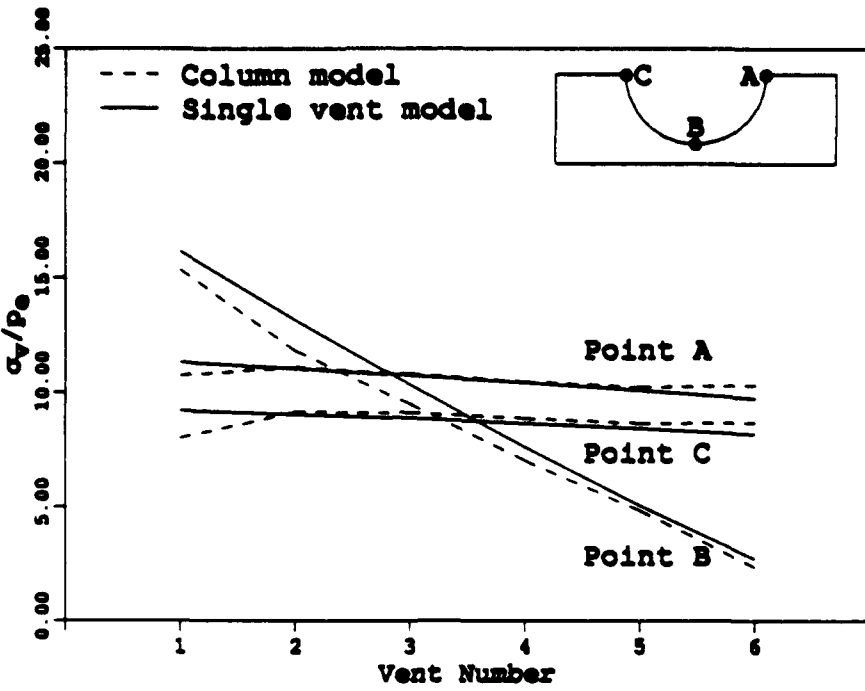


FIGURE 9. COMPARISON OF THE VON MISES STRESS FOR BOTH MODELS. VENT NUMBER 1 IS AT BRAKE ENTRANCE.
 $r_o/r_b = 1.35$, $n_c = 12$, $d/s_c = 0.66$, and $d/x_c = 0.50$.

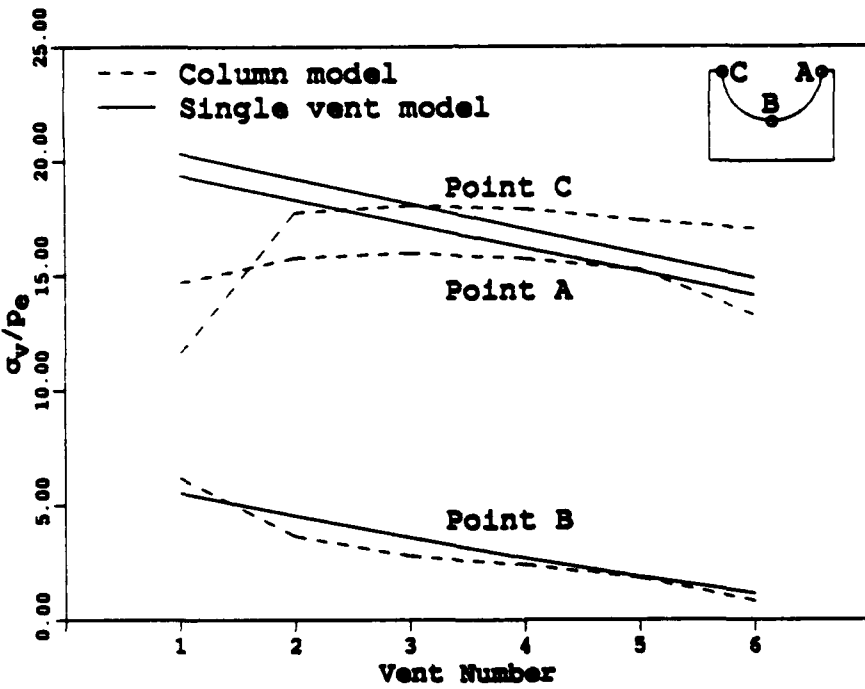


FIGURE 10. COMPARISON OF THE VON MISES STRESS FOR BOTH MODELS. VENT NUMBER 1 IS AT BRAKE ENTRANCE.
 $r_o/r_b = 1.35$, $n_c = 12$, $d/s_c = 0.47$, and $d/x_c = 0.80$.

TECHNICAL REPORT INTERNAL DISTRIBUTION LIST

	<u>NO. OF COPIES</u>
CHIEF, DEVELOPMENT ENGINEERING DIVISION	
ATTN: SMCAR-CCB-DA	1
-DC	1
-DI	1
-DR	1
-DS (SYSTEMS)	1
CHIEF, ENGINEERING DIVISION	
ATTN: SMCAR-CCB-S	1
-SD	1
-SE	1
CHIEF, RESEARCH DIVISION	
ATTN: SMCAR-CCB-R	2
-RA	1
-RE	1
-RM	1
-RP	1
-RT	1
TECHNICAL LIBRARY	
ATTN: SMCAR-CCB-TL	5
TECHNICAL PUBLICATIONS & EDITING SECTION	
ATTN: SMCAR-CCB-TL	3
OPERATIONS DIRECTORATE	
ATTN: SMCWV-ODP-P	1
DIRECTOR, PROCUREMENT & CONTRACTING DIRECTORATE	
ATTN: SMCWV-PP	1
DIRECTOR, PRODUCT ASSURANCE & TEST DIRECTORATE	
ATTN: SMCWV-QA	1

NOTE: PLEASE NOTIFY DIRECTOR, BENÉT LABORATORIES, ATTN: SMCAR-CCB-TL OF ADDRESS CHANGES.

TECHNICAL REPORT EXTERNAL DISTRIBUTION LIST

<u>NO. OF COPIES</u>	<u>NO. OF COPIES</u>		
ASST SEC OF THE ARMY RESEARCH AND DEVELOPMENT ATTN: DEPT FOR SCI AND TECH THE PENTAGON WASHINGTON, D.C. 20310-0103	1	COMMANDER ROCK ISLAND ARSENAL ATTN: SMCR-ENM ROCK ISLAND, IL 61299-5000	1
ADMINISTRATOR DEFENSE TECHNICAL INFO CENTER ATTN: DTIC-FDAC CAMERON STATION ALEXANDRIA, VA 22304-6145	12	MIAC/CINDAS PURDUE UNIVERSITY P.O. BOX 2634 WEST LAFAYETTE, IN 47906	1
COMMANDER U.S. ARMY ARDEC ATTN: SMCAR-AEE SMCAR-AES, BLDG. 321 SMCAR-AET-O, BLDG. 351N SMCAR-CC SMCAR-FSA SMCAR-FSM-E SMCAR-FSS-D, BLDG. 94 SMCAR-IMI-I, (STINFO) BLDG. 59	1	COMMANDER U.S. ARMY TANK-AUTMV R&D COMMAND ATTN: AMSTA-DDL (TECH LIBRARY) WARREN, MI 48397-5000	1
PICATINNY ARSENAL, NJ 07806-5000	2	COMMANDER U.S. MILITARY ACADEMY ATTN: DEPARTMENT OF MECHANICS WEST POINT, NY 10966-1792	1
DIRECTOR U.S. ARMY RESEARCH LABORATORY ATTN: AMSRL-DD-T, BLDG. 305 ABERDEEN PROVING GROUND, MD 21005-5066	1	U.S. ARMY MISSILE COMMAND REDSTONE SCIENTIFIC INFO CENTER ATTN: DOCUMENTS SECTION, BLDG. 4484 REDSTONE ARSENAL, AL 35898-5241	2
DIRECTOR U.S. ARMY RESEARCH LABORATORY ATTN: AMSRL-WT-PD (DR. B. BURNS) ABERDEEN PROVING GROUND, MD 21005-5066	1	COMMANDER U.S. ARMY FOREIGN SCI & TECH CENTER ATTN: DRXST-SD 220 7TH STREET, N.E. CHARLOTTESVILLE, VA 22901	1
DIRECTOR U.S. MATERIEL SYSTEMS ANALYSIS ACTV ATTN: AMXSY-MP ABERDEEN PROVING GROUND, MD 21005-5071	1	COMMANDER U.S. ARMY LABCOM MATERIALS TECHNOLOGY LABORATORY ATTN: SLCMT-IML (TECH LIBRARY) WATERTOWN, MA 02172-0001	2
		COMMANDER U.S. ARMY LABCOM, ISA ATTN: SLCIS-IM-TL 2800 POWER MILL ROAD ADELPHI, MD 20783-1145	1

NOTE: PLEASE NOTIFY COMMANDER, ARMAMENT RESEARCH, DEVELOPMENT, AND ENGINEERING CENTER, U.S. ARMY AMCCOM, ATTN: BENET LABORATORIES, SMCAR-CCB-TL, WATERVLIET, NY 12189-4050 OF ADDRESS CHANGES.

TECHNICAL REPORT EXTERNAL DISTRIBUTION LIST (CONT'D)

	<u>NO. OF</u> <u>COPIES</u>		<u>NO. OF</u> <u>COPIES</u>
COMMANDER U.S. ARMY RESEARCH OFFICE ATTN: CHIEF, IPO P.O. BOX 12211 RESEARCH TRIANGLE PARK, NC 27709-2211	1	COMMANDER AIR FORCE ARMAMENT LABORATORY ATTN: AFATL/MN EGLIN AFB, FL 32542-5434	1
DIRECTOR U.S. NAVAL RESEARCH LABORATORY ATTN: MATERIALS SCI & TECH DIV CODE 26-27 (DOC LIBRARY) WASHINGTON, D.C. 20375	1	COMMANDER AIR FORCE ARMAMENT LABORATORY ATTN: AFATL/MNF EGLIN AFB, FL 32542-5434	1

NOTE: PLEASE NOTIFY COMMANDER, ARMAMENT RESEARCH, DEVELOPMENT, AND ENGINEERING CENTER, U.S. ARMY AMCCOM, ATTN: BENET LABORATORIES, SMCAR-CCB-TL, WATERVLIET, NY 12189-4050 OF ADDRESS CHANGES.
